Journal of Natural Resources and Farming
https://doi.org/10.7770/jonraf-v2-art2909

SPECIAL ISSUE

Historical intensity and predictive uncertainty of extreme maximum temperatures in south-central Chile: An integrated approach using the H_S^{obs} and I_G^{pred} indices

William Campillay-Llanos[a*], Patricio González-Colville[b], Marlon M. López-Flores[c]

Núcleo de Investigación en Producción Alimentaria, Facultad de Recursos Naturales, Universidad Católica de Temuco, Temuco[a], Chile
Research and Extension Center for Irrigation and Agroclimatology (CITRA), Universidad de Talca, Campus Lircay, Talca[b], Chile
Artificial Intelligence, Robotics and Cybernetics Laboratory (LIARC), Military Institute of Engineering, Rio de Janeiro[c], Brazil

Article history
Received: 10/02/2026
Accepted: 20/07/2026
Published: 22/09/2026

Corresponding author
*William Campillay-Llanos
williamcampillay@gmail.cl

ABSTRACT
This study proposes an integrated approach for characterising extreme maximum temperatures through two complementary indicators: the observed summer extreme heat-load index (H_s^{obs}) and the predictive geometric index (I_G^{pred}). The former summarises the historical intensity of absolute maximum temperatures recorded in December, January, February, and March during 2000–2026. Its exponential weighting assigns progressively more importance to the most intense thermal events. The latter quantifies the relative width of the 2026–2030 prediction bands within a common thermal domain, thereby providing a dimensionless measure for comparing predictive uncertainty among locations. The method is applied to Temuco, Los Ángeles, Chillán, Talca, Curicó, Santiago Quinta Normal, and Santiago Pudahuel. The joint representation (I_G^{pred}, H_s^{obs}) contrasts the historical burden of extreme heat with the width of future predictive uncertainty. Los Ángeles exhibits the greatest historical heat load, whereas Temuco combines a relatively low load with the widest prediction band. Chillán and Talca occupy intermediate positions, confirming that thermal intensity and predictive uncertainty describe distinct, non-equivalent dimensions of climate behaviour. The proposed indices provide a comparative agroclimatological tool; however, H_s^{obs} is a relative climate indicator rather than a direct measure of physiological damage, which would require system-specific experimental calibration.

Keywords: agroclimatology; extreme maximum temperature; heat load; prediction band; geometric index; thermal sensitivity.

1. Introduction

Recent evidence has shown that exposure to hourly heat extremes is increasing unequally across regions and generations, highlighting the need for high-resolution assessments of extreme heat and its societal and environmental implications (Liao et al., 2026). In this context, absolute maximum temperature is a relevant variable for characterising the temporal evolution of the most intense thermal episodes and assessing their potential agroclimatological implications. Its analysis is particularly important because increasingly frequent and intense heat extremes may progressively become part of the prevailing climatic conditions, affecting organismal physiology, behaviour, species distributions, and the functioning of agricultural systems (Ellis-Soto et al., 2026). Its analysis is particularly important because changes in temperature extremes do not necessarily mirror changes in mean temperature, while extreme heat can produce substantial consequences for human populations, ecosystems, and other climate-sensitive systems (White et al., 2023). Using meteorological data provided and agroclimatologically curated by Patricio González-Colville, previous analyses of historical trends and future scenarios in central-southern Chile have demonstrated that maximum summer temperatures provide a robust basis for assessing spatial differences in the evolution of thermal extremes (Campillay-Llanos et al., 2024).

The intensity of a thermal extreme and its predictive uncertainty are, nevertheless, different concepts. The former describes how high a temperature may become, whereas the latter describes the width of the set of values compatible with a prediction. Two locations may therefore show similar thermal trends while exhibiting prediction bands with different widths and different proximities to agroclimatologically relevant thresholds.

This study combines a geometric measure of predictive-band width with an exponentially weighted measure of observed summer extremes. The objective is to separate and jointly interpret historical extreme-heat intensity and future predictive uncertainty across seven locations in central and south-central Chile. In this context, the analysis of extreme maximum temperatures is relevant, for example, to understanding their relationship with the cardinal temperatures that determine the thermal response of *Botrytis cinerea*. The infection risk associated with this pathogen has been described using thermal performance curves defined by minimum (T_{min}), optimum (T_{opt}), and maximum (T_{max}) temperatures (Campillay-Llanos et al., 2025). Consequently, historical and projected changes in maximum temperatures may modify the frequency with which environmental conditions approach or exceed these thresholds, particularly the upper thermal limit. Characterising these changes may improve the spatial and temporal identification of conditions favourable for infection and contribute to a more accurate assessment of phytosanitary risk. The proposed approach may also support the identification of sweet cherry orchards requiring timely thermal protection measures. In particular, the indices may help identify greater heat exposure and uncertainty during floral-bud development, when high temperatures can promote double fruits and deep sutures (Fundación para la Innovación Agraria, 2021).

Thus, the proposed indices complement process-based and technological approaches by quantifying thermal exposure and predictive dispersion.

2. Materials and methods

The methodological framework follows previous studies based on historical records of daily maximum air temperature and projections of absolute maximum summer temperatures in central and south-central Chile (Campillay-Llanos et al., 2024, 2025). For each meteorological station and year, the highest daily temperature recorded in December, January, February, and March was extracted. These monthly absolute maxima were used to construct the historical extreme-temperature series, estimate its temporal trend, and generate future predictions. These months were selected because they concentrate the most intense summer heat events in the study area. Previous applications of this methodology have documented a sustained increase in extreme maximum temperatures.

3. Temporal Patterns of Extreme Maximum Temperatures

Figures 1-7 show the temporal distribution of the absolute maximum temperatures recorded during January, February, March, and December between 2000 and 2026. A common colour scale was applied to all locations to facilitate direct spatial and temporal comparisons. Lighter colours indicate lower absolute maximum temperatures, whereas darker red tones represent more intense thermal extremes. The grey cell corresponding to December 2026 indicates that this observation was unavailable.

3.1 Predictive geometric index

For each location, T_{p5} and T_{p95} denote the 5th and 95th percentiles, respectively, of the predicted distribution of absolute maximum temperatures. These limits define the prediction band used to quantify future thermal uncertainty. Let $[T^D_{\min}, T^D_{\max}]$ represent the common thermal reference domain applied to all locations. The predictive geometric index is defined as

$$I_G^{\text{pred}} = \frac{T_{p95} - T_{p5}}{T^D_{\max} - T^D_{\min}}. \tag{1}$$

The index represents the fraction of the common thermal domain occupied by the prediction band. Larger values indicate greater predictive dispersion, whereas smaller values indicate more concentrated predictions. Because the same

Figure 1.

Temporal heatmap of absolute maximum temperatures at the Santiago–Quinta Normal station from 2000 to 2026. The figure represents the highest temperatures recorded during January, February, March, and December of each year. The common colour scale allows direct comparison with the other locations included in the study.

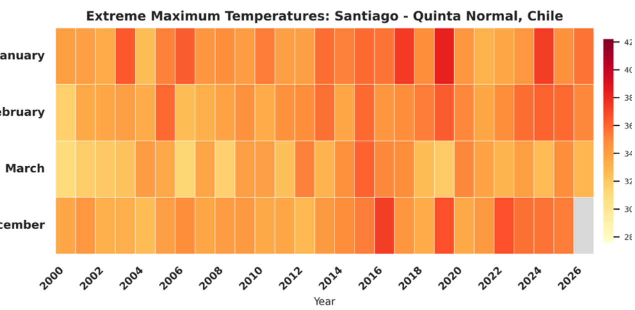

Figure 2.

Temporal heatmap of absolute maximum temperatures at the Santiago–Pudahuel station from 2000 to 2026. Darker colours identify years and months characterised by more intense maximum temperatures, allowing the occurrence of extreme thermal events in western Santiago to be examined.

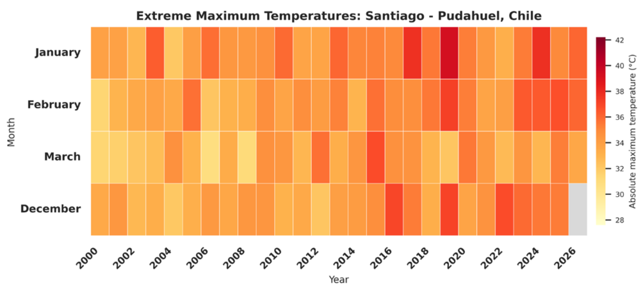

Figure 3.

Temporal heatmap of absolute maximum temperatures in Curicó from 2000 to 2026. The monthly distribution illustrates the interannual variability of summer temperature extremes and facilitates comparison with the northern and southern locations considered in the study.

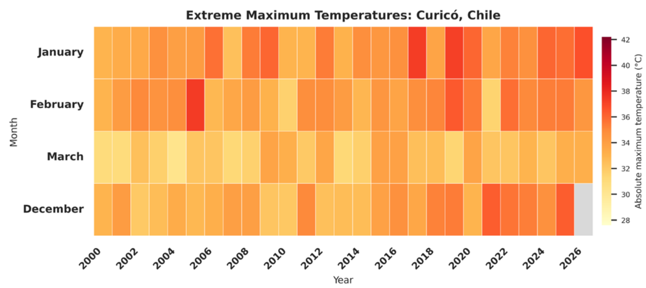

Figure 4.

Temporal heatmap of absolute maximum temperatures in Talca from 2000 to 2026. The colour intensity describes the magnitude of the thermal extremes observed during January, February, March, and December, highlighting their temporal variability across the study period.

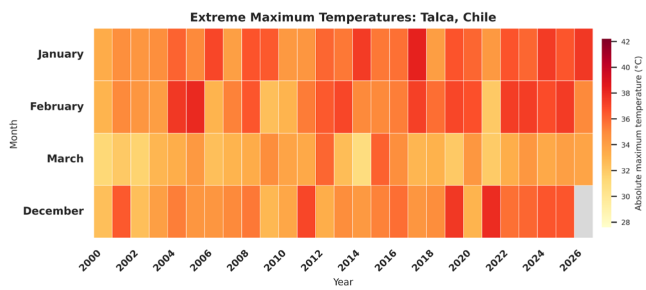

Figure 5.

Temporal heatmap of absolute maximum temperatures in Chillán from 2000 to 2026. Darker red cells indicate the occurrence of comparatively intense thermal extremes, particularly during January and February, while lighter colours represent lower maximum-temperature conditions.

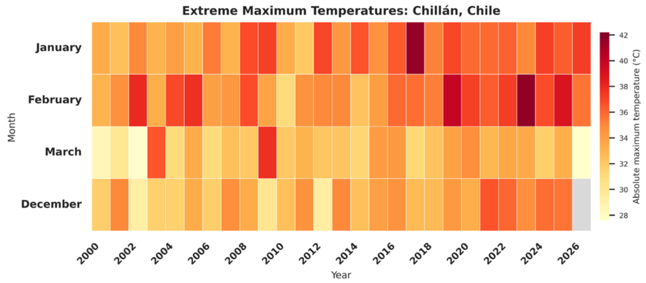

Figure 6.

Temporal heatmap of absolute maximum temperatures in Los Ángeles from 2000 to 2026. The figure shows the monthly and interannual distribution of temperature extremes and highlights episodes of particularly high thermal intensity during the austral summer.

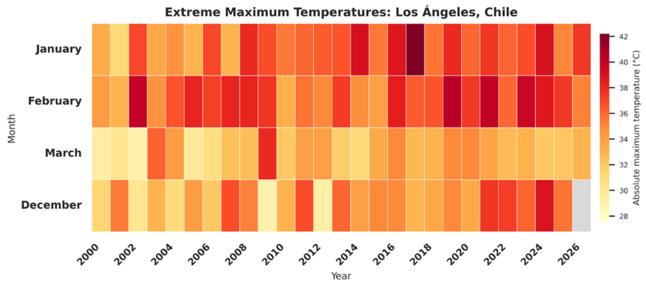

Figure 7.

Temporal heatmap of absolute maximum temperatures in Temuco, Chile, from 2000 to 2026. The figure shows the monthly and interannual variability of thermal extremes recorded during January, February, March, and December. Darker red tones indicate higher absolute maximum temperatures, whereas lighter colours represent less intense thermal conditions. The grey cell indicates that the observation for December 2026 was unavailable.

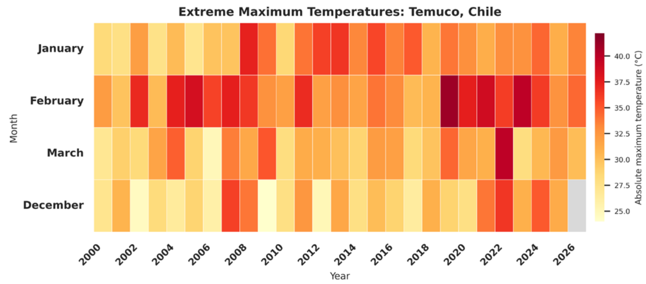

reference domain is used for all locations, I_G^{pred} provides a dimensionless measure that enables direct spatial comparison.

The index quantifies predictive dispersion rather than extreme-temperature intensity. It must therefore be interpreted jointly with the observed historical trends and predicted temperature levels. Furthermore, it complements, but does not replace, statistical coverage assessment, residual diagnostics, and out-of-sample validation.

3.2 Observed summer extreme heat-load index

Thermal Death Time (TDT) and Thermal Load Sensitivity (TLS) models relate the intensity and duration of thermal exposure to biological responses, providing a cumulative framework that extends beyond the use of a single critical temperature threshold (Rezende et al., 2014, 2020; Cook et al., 2024). Noble et al. (2026) express accumulated heat injury as

$$HI(t) = 100 \int_0^t 10^{\frac{T(i) - CT_{\max,1\text{h}}}{z}} \, di, \tag{2}$$

where $T(i)$ is the temperature trajectory, z is thermal sensitivity, and $CT_{\max,1\text{h}}$ is the static temperature at which 50% of the population reaches the assessed endpoint after one hour of exposure. A larger z denotes lower sensitivity because a greater temperature increment is required to reduce tolerance time by a factor of ten.

The data used here consist of absolute maximum temperatures rather than continuous hourly trajectories. Equation (2) is therefore not used as a direct estimate of injury. Its exponential structure is retained to construct a discrete indicator of the relative load associated with observed summer maximum-temperature extremes:

$$H_{S,j}^{\text{obs}} = \frac{1}{N_j} \sum_{i=1}^{N_j} 10^{\frac{T_{\max,j,i} - T_{\text{ref}}}{z_S}}. \tag{3}$$

Here, $T_{\max,j,i}$ is the ith observed absolute maximum temperature at location j, T_{ref} is a reference temperature, z_S controls the sensitivity of the transformation, and N_j is the number of available observations. The analysis uses December, January, February, and March maxima from 2000 to 2026. Because December 2026 was unavailable, $N_j = 26(4) + 3 = 107$ observations were used per location. The exploratory reference scenario is

$$T_{\text{ref}} = 35\,^{\circ}\text{C}, \qquad z_S = 5\,^{\circ}\text{C}. \tag{4}$$

Accordingly,

$$H_{S,j}^{\text{obs}} = \frac{1}{107} \sum_{i=1}^{107} 10^{\frac{T_{\max,j,i} - 35}{5}}. \tag{5}$$

Normalisation by N_j expresses the index as the mean relative thermal load, thereby preventing its magnitude from depending solely on sample size. This normalisation is conceptually inspired by the framework proposed by (2026).

3.3 Interpretation of H_S^{obs}

The reference contribution is equal to one when $T_{max} = T_{ref}$. Thus, $H_S^{obs} \approx 1$ indicates that mean thermal load is close to the reference condition on the scale of the indicator. Values above or below one indicate greater or lower relative load, respectively.

The exponential structure gives exceptionally warm events progressively greater weight. With $T_{ref} = 35$ °C and $z_S = 5$ °C, an observed maximum of 35 °C contributes $10^{(35-35)/5} = 1$, whereas 40 °C contributes $10^{(40-35)/5} = 10$. A 40 °C event therefore receives ten times the weight of anobservation at the reference temperature.

The indicator does not directly represent mortality, physiological injury, or yield loss. Biological interpretation would require calibration of T_{ref}, z_S, and potentially a critical temperature against experimental data for the crop and phenological stage of interest.

3.4 Joint historical–predictive representation

The two indices describe different temporal and conceptual dimensions:

$$\begin{aligned} H_S^{obs} &\longrightarrow \text{historical summer extreme-heat load,} \\ I_G^{pred} &\longrightarrow \text{future predictive-band width.} \end{aligned} \tag{6}$$

Each location is therefore represented by

$$\left(I_{G,j}^{pred}, H_{S,j}^{obs}\right). \tag{7}$$

This plane distinguishes locations with a high historical heat load but moderate predictive uncertainty from locations with a lower historical load and a considerably wider future prediction band.

4. Results

4.1 Prediction-band width

Table I summarises the indicators used to characterise the magnitude and temporal evolution of extreme maximum temperatures, evaluate the goodness of fit of the estimated trends, and quantify predictive uncertainty. Together, these measures distinguish observed thermal intensity and trend behaviour from the empirical coverage, mean width, and geometric extent of the prediction bands.

Figure 8 subsequently compares the relative width of these prediction bands using a common thermal scale. Santiago Quinta Normal and Santiago Pudahuel exhibit the most concentrated bands, whereas Curicó and Talca show intermediate values. Chillán, Los Ángeles, and particularly Temuco present wider prediction bands. This ordering describes predictive width and should not be interpreted as the probability of reaching a particular temperature or as the magnitude of the expected extreme.

Table I

Indicators used to assess trends and predictive uncertainty in extreme maximum temperatures.

Indicator	Question addressed
TXx	What was the extreme maximum temperature?
Slope, $\hat{\beta}_1$	How rapidly are extremes changing over time?
Coefficient of determination, R^2	How much variability is explained by the temporal trend?
Residual standard deviation	How far do observations deviate from the fitted trend?
Empirical coverage	What proportion of observations falls within the prediction band?
Mean width	How wide are the prediction intervals on average?
Geometric index, I_G	What fraction of a common climate domain is occupied by the entire prediction band?

4.2 Historical heat load and predictive uncertainty

Table II presents the two indices. Los Ángeles has the largest H_S^{obs} (2.163), followed by Chillán (1.485) and Talca (1.271). Temuco has a value near the reference level (0.934) but the largest I_G (89.34%). These results demonstrate that historical intensity and future predictive width are not redundant.

Table II

Geometric index (I_G) and observed summer extreme heat-load index (H_S^{obs}). Both indicators were calculated from 107 absolute maximum temperatures recorded during January, February, March, and December over the period 2000–2026. The geometric index was computed over the common thermal domain 25–45 °C, whereas H_S^{obs} was calculated using $T_{ref} = 35$ °C and $z_S = 5$ °C.

Location	I_G (%)	H_S^{obs}
Santiago Quinta Normal	23.40	0.909
Santiago Pudahuel	24.20	0.979
Curicó	24.40	0.747
Talca	27.40	1.271
Chillán	38.70	1.485
Los Ángeles	44.90	2.163
Temuco	55.40	0.934

4.3 Crop-area context

Figures 10 and 11 integrate the climatic indicators I_G and H_S^{obs} with the regional planted areas of sweet cherry and European hazelnut, respectively. These crops were selected because of their economic importance, expanding cultivation, and broad distribution across south-central Chile, where they represent contrasting territorial patterns of fruit production under increasingly relevant summer thermal extremes. Each location is positioned according to the relative spread of its

Figure 8.

Geometric index (I_G) and thermal exposure across the analysed locations. Horizontal segments represent the empirical *p*5–*p*95 intervals calculated from 107 summer absolute maximum temperatures recorded during 2000–2026. The index $I_G = (p95 - p5)/(45 - 25)$ measures the fraction of the common 25–45 °C thermal domain occupied by the central 90 % of the observations. Dashed vertical lines provide thermal context: the 15–25 °C range represents conditions favourable to Botrytis cinerea, whereas 40 and 45 °C contextualise increasing heat stress and extreme heat in sweet cherry, respectively. The most critical absolute maxima were recorded in Los Ángeles (42.2 °C), Chillán (41.6 °C), and Temuco (41.1 °C). Although these values exceed 40 °C, the corresponding *p*95 values remain below this threshold, indicating that they represent infrequent extreme events rather than the upper limit of the central 90 % of the observations.

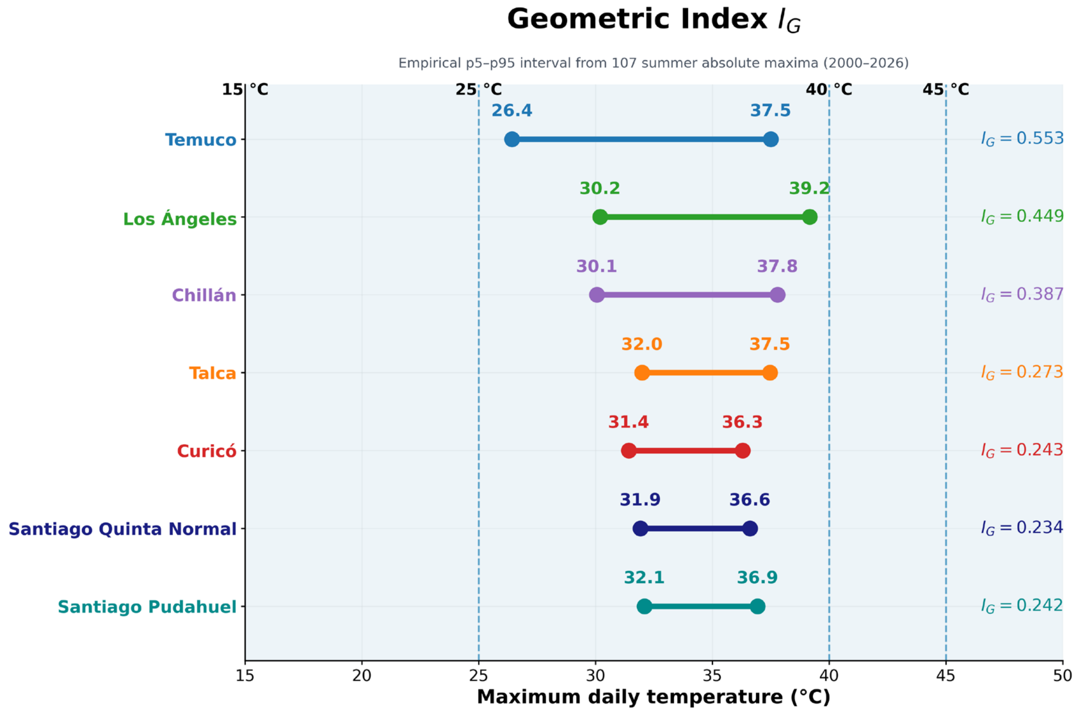

Figure 9.

Observed summer extreme heat load (H_S^{obs}) versus the predictive geometric index (I_G^{pred}). Upward displacement indicates a greater historical heat load, whereas rightward displacement indicates a wider prediction band and greater predictive uncertainty.

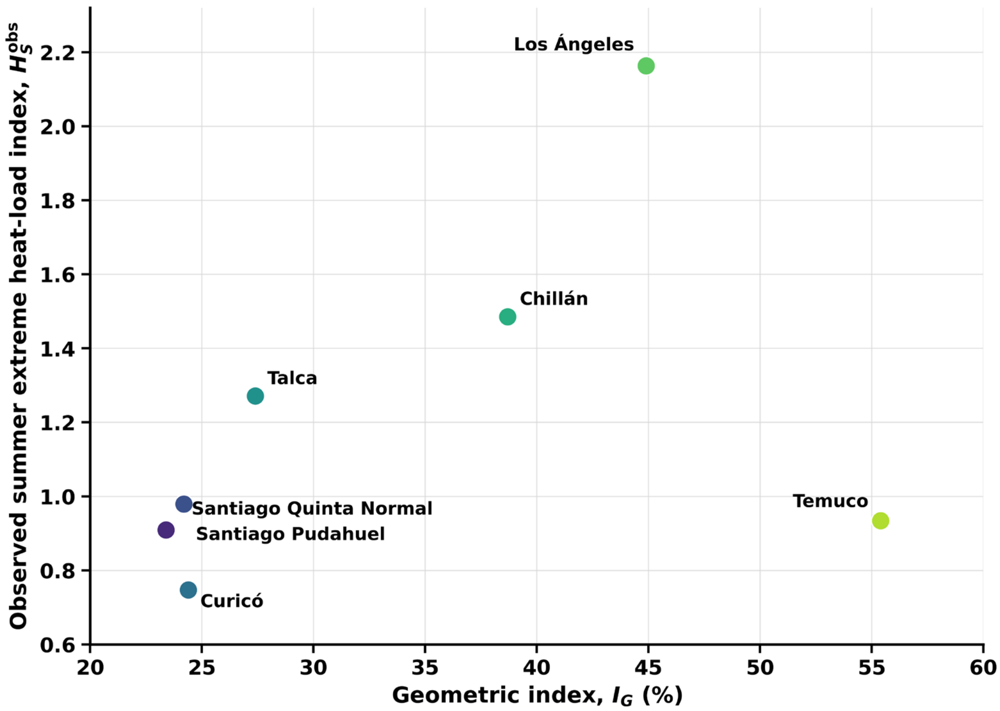

Figure 10.

I_G^{pred} versus H_S^{obs} for the seven locations, with bubble area proportional to regional sweet-cherry planted area. The plot simultaneously identifies high historical heat load, wide predictive uncertainty, and territorial concentration of production.

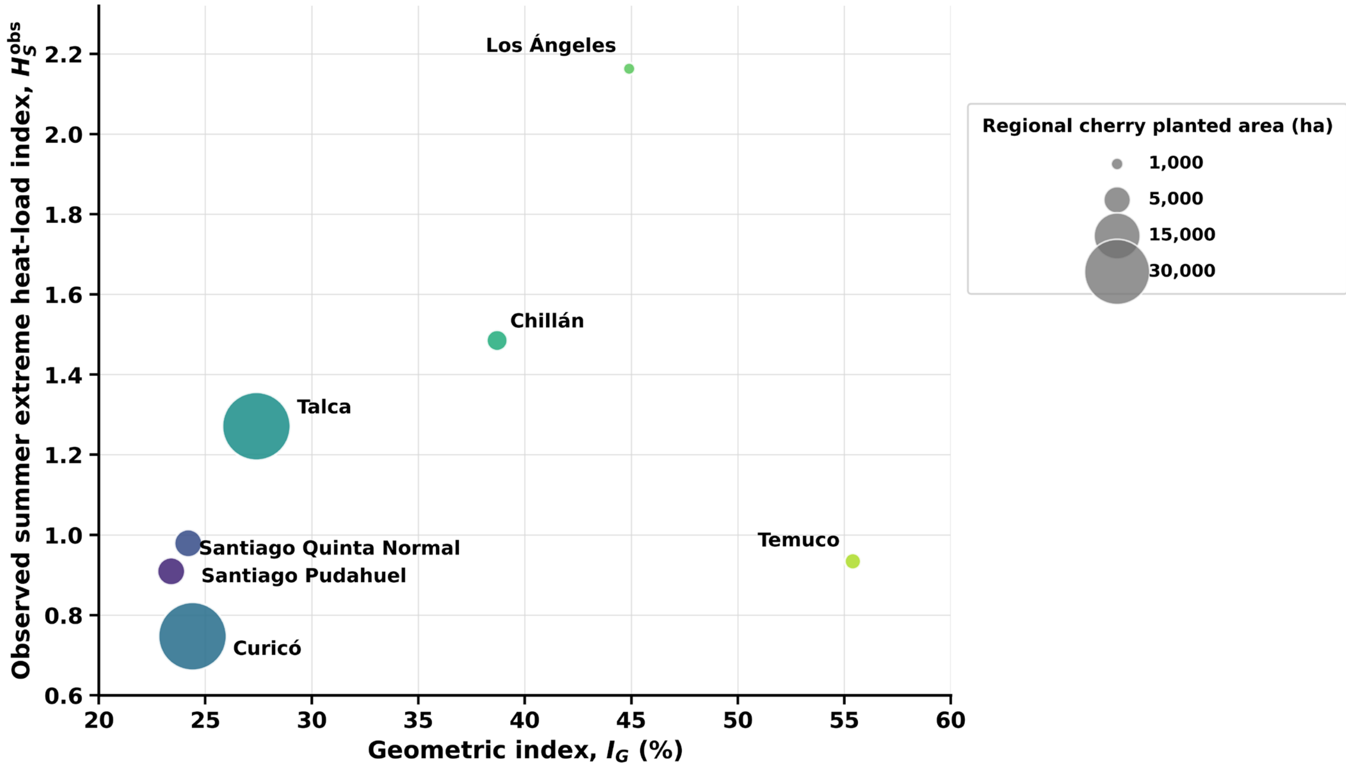

Figure 11.

I_G^{pred} versus H_S^{obs}, with bubble area proportional to the regional planted area of European hazelnut (*Corylus avellana L.*).

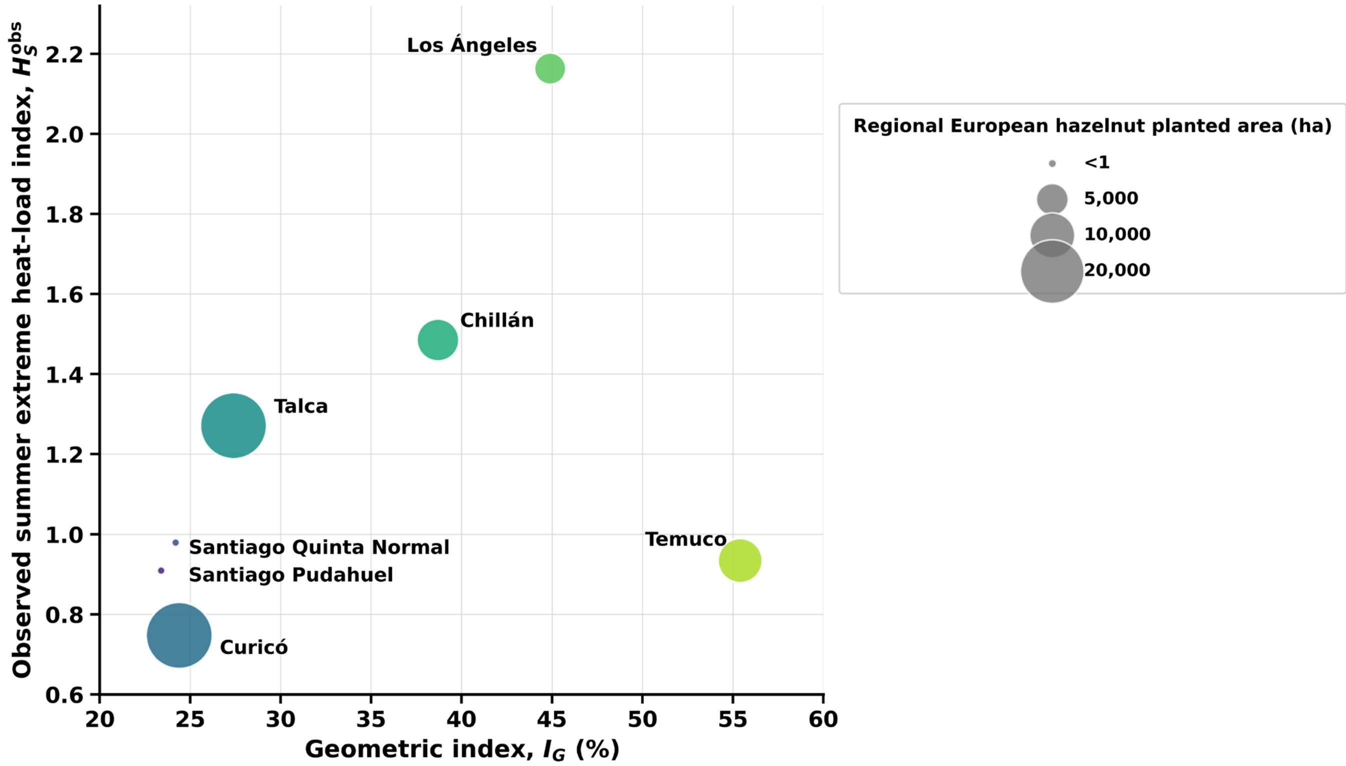

Figure 12.

Sensitivity of H_S^{obs} to z_S for $T_{ref} = 35$ °C. Smaller z_S values amplify the weight of the most intense thermal events. Los Ángeles and Chillán retain the two highest relative heat loads throughout the analysed interval.

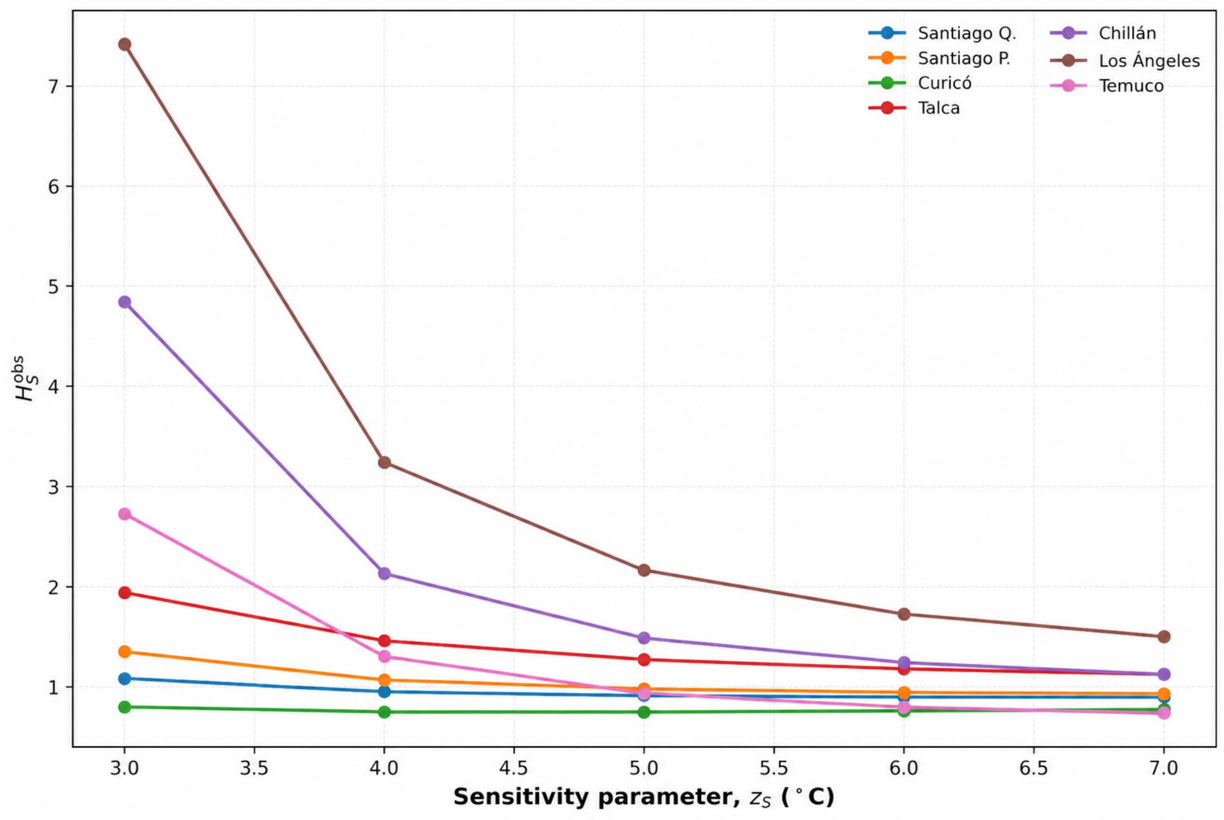

Figure 13.

Stability of the spatial ordering according to H_S^{obs}. Spearman's rank correlation compares each z_S scenario with the reference scenario $z_S = 5$ °C.

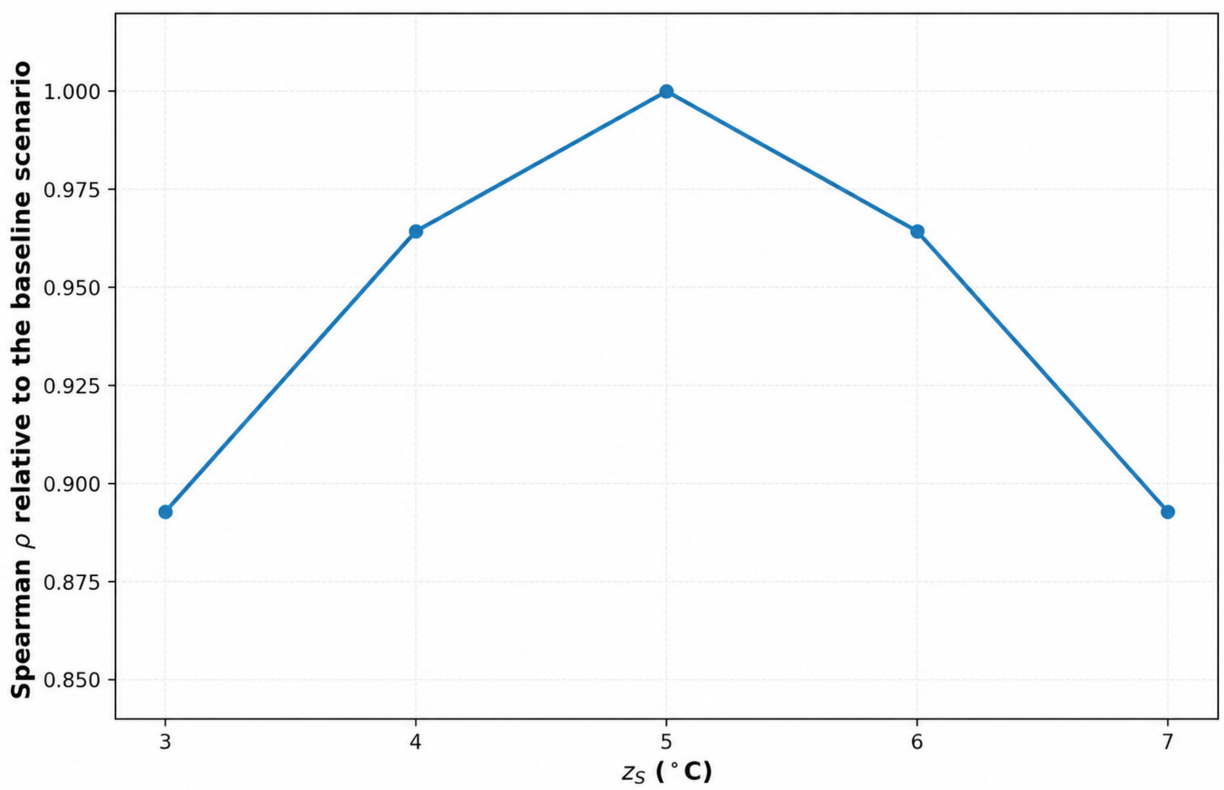

extreme maximum temperatures and its observed summer heat load, while bubble area represents the regional planted area of the corresponding crop. This representation identifies regions where particular thermal conditions coincide with a greater concentration of cultivated land, thereby providing a production-oriented context for prioritising climate monitoring and crop-specific adaptation studies. Nevertheless, planted area does not modify either index and should not be interpreted as a direct measure of physiological damage, yield loss, or economic risk.

5. Sensitivity analysis of H_S^{obs}

Because H_S^{obs} depends on T_{ref} and z_S, a sensitivity analysis was conducted using $T_{ref} \in \{33, 34, 35, 36, 37\}$ °C and $z_S \in \{3, 4, 5, 6, 7\}$ °C.

5.1 Effect of the reference temperature

Equation (3) can be factorised as

$$H^{\text{obs}}_{S,j}(T_{\text{ref}}, z_S) = 10^{-T_{\text{ref}}/z_S} \left[\frac{1}{N_j} \sum_{i=1}^{N_j} 10^{T_{\max,j,i}/z_S} \right]. \quad (8)$$

For fixed z_S, changing the reference temperature by ΔT gives

$$H^{\text{obs}}_{S,j}(T_{\text{ref}} + \Delta T, z_S) = 10^{-\Delta T/z_S} H^{\text{obs}}_{S,j}(T_{\text{ref}}, z_S). \quad (9)$$

Because this multiplicative factor is identical for every location, T_{ref} changes the magnitude of the indicator but not the ranking of locations for a fixed z_S.

5.2 Sensitivity to z_S

Smaller z_S values increase the weight assigned to the highest temperatures, whereas larger values smooth the response and reduce absolute differences among locations. Table III reports representative scenarios.

Table III

Sensitivity of H_S^{obs} to z_S. The position column gives the range of ranks occupied by each location over $z_S \in [3, 7]$,° C.

Location	$H_S(3)$	$H_S(5)$	$H_S(7)$	Position
Santiago Quinta Normal	1.085	0.909	0.894	5–6
Santiago Pudahuel	1.350	0.979	0.930	4–5
Curicó	0.799	0.747	0.772	6–7
Talca	1.938	1.271	1.123	3–4
Chillán	4.842	1.485	1.125	2–2
Los Ángeles	7.418	2.163	1.501	1–1
Temuco	2.728	0.934	0.736	3–7

Los Ángeles remains first and Chillán second throughout the sensitivity range. Temuco shows the greatest ordinal sensitivity, moving between third and seventh place because its generally moderate maxima coexist with isolated high extremes.

5.3 Stability of the spatial ranking

Spearman's rank correlation (ρ) was calculated between the ordering under each z_S scenario and the reference ordering at $z_S = 5$ °C:

$$\begin{array}{c|ccccc} z_S\ (^\circ\text{C}) & 3 & 4 & 5 & 6 & 7 \\ \hline \rho & 0.893 & 0.964 & 1.000 & 0.964 & 0.893 \end{array}. \quad (10)$$

The correlations remain between 0.893 and 1.000, indicating strong preservation of the overall spatial ordering.

6. Discussion

The results distinguish sensitivity in indicator magnitude from robustness of the spatial pattern. The absolute magnitude of H_S^{obs} can vary substantially with z_S, particularly where exceptionally high thermal events occur. Nevertheless, the principal spatial differences remain stable: Los Ángeles and Chillán consistently show the greatest historical loads.

The geometric index adds a separate dimension. Temuco, for example, does not have the largest historical heat load, but it has the widest relative prediction band. Conversely, a location may have experienced high historical extremes while retaining moderate predictive width. The joint representation therefore prevents predictive precision from being confused with thermal severity.

The approach can support comparisons among weather stations, models, periods, and climate scenarios, while providing a dimensionless representation of predictive uncertainty. For sweet cherry and European hazelnut, the joint use of I_G^{pred} and H_S^{obs} can help identify production areas where substantial historical heat loads coincide with wider predictive ranges, thereby supporting the spatial prioritisation of monitoring and adaptation studies. Crop-specific risk assessment, however, requires phenological information and experimentally determined thermal-tolerance data.

The principal limitation is that H_S^{obs} is inspired by the mathematical structure of TDT/TLS models but is calculated from absolute maxima rather than continuous exposures. It must not be interpreted as an estimate of injury or mortality. Likewise, I_G^{pred} measures relative band width rather than coverage probability. Further work should calibrate the heat load parameters for specific crops, test alternative reference domains, and validate the prediction bands using out-of-sample data.

7. Conclusions

The combined indices distinguish two complementary dimensions of extreme maximum temperature. H_S^{obs} summarises historical summer heat load by emphasising exceptionally warm events, whereas I_G^{pred} quantifies the relative width of future prediction bands within a common thermal domain.

Among the seven locations, Los Ángeles exhibits the greatest historical heat load, while Temuco presents the greatest predictive width. Santiago Quinta Normal and Santiago Pudahuel show the most concentrated prediction bands. The sensitivity analysis confirms that, although the magnitude of H_S^{obs} depends on z_S, the main spatial ordering remains robust.

This dimensionless framework supports spatial comparisons of historical heat intensity and future predictive uncertainty. It may also support the modelling and projection of cardinal temperatures associated with pathogen infection rates and practical applications such as planning and evaluating solar protectants in fruit orchards. Nevertheless, crop-, pathogen-, and phenological-stage-specific interpretations require experimental calibration.

Acknowledgements

Research support provided by NIPA–Universidad Católica de Temuco and CITRA–Universidad de Talca. M.M.L.-F. received partial funding from project EVAAT-GCN under FINEP agreement 01.24.0661.00, ref. 3311/24.

Author contributions

Conceptualisation, methodology, formal analysis, writing—original draft, and writing—review and editing: P.G.-C. and W.C.-L.; formal analysis and writing—review and editing: M.M.L.-F. All authors reviewed and approved the final version of the manuscript.

Declaration on the Use of Artificial Intelligence

The authors used ChatGPT (OpenAI) solely to improve the writing and review Python code. All scientific content was verified by the authors, who assume full responsibility for the manuscript.

Data Availability Statement

The meteorological data used in this study are available from the authors upon reasonable request for scientific research purposes.

Declaration of competing interests

The authors declare no competing interests.

References

A. M. Cook, E. L. Rezende, K. Petrou, and A. Leigh (2024) Beyond a single temperature threshold: Applying a cumulative thermal stress framework to plant heat tolerance, *Ecology Letters*, **27**(3), e14416.

D. Ellis-Soto, D. W. Noble, P. A. Arnold, P. Pottier, A. J. Robey, C. Prokopenko, and J. Cohen (2026) Extreme heat as the new normal: A methodological roadmap incorporating behavior, physiology, and species distributions, *Integrative and Comparative Biology*, icag045.

D. W. A. Noble, P. A. Arnold, S. Nakagawa, and P. Pottier (2026) A flexible modelling framework for estimating thermal tolerance and sensitivity, *bioRxiv*.

E. L. Rezende, L. E. Castañeda, and M. Santos (2014) Tolerance landscapes in thermal ecology, *Functional Ecology*, **28**(4), 799–809.

E. L. Rezende, F. Bozinovic, A. Szilágyi, and M. Santos (2020) Predicting temperature mortality and selection in natural *Drosophila* populations, *Science*, **369**(6508), 1242–1245.

Fundación para la Innovación Agraria (FIA), Desarrollo y validación de un protector solar novedoso con componentes activos para disminuir el estrés térmico por calor en yemas florales y reducir la producción de frutos dobles y/o con sutura profunda en huertos de cerezo dulce (*Prunus avium* L.), Proyecto FIA PYT-2021-0543, Centro de Estudios Avanzados en Fruticultura (CEAF), Región de O'Higgins, Chile, 2021–2024. Available at: https://opia.fia.cl/601/w3-article-118620.html.

R. H. White, S. Anderson, J. F. Booth, G. Braich, C. Draeger, C. Fei, et al. (2023) The unprecedented Pacific Northwest heatwave of June 2021, *Nature Communications* **14**(1), 727.

W. Campillay-Llanos, P. González-Colville, S. Ortega-Farías, and M. M. López-Flores (2024) Historical trends and future scenario projection of maximum summer temperatures in the Southern Hemisphere: Central-southern zone of Chile, *Idesia*, **42**(3), 43–54.

W. Campillay-Llanos, S. Ortega-Farías, P. González-Colville, G. A. Díaz, M. M. López-Flores, and R. López-Olivari (2025) Modeling the effects of extreme temperatures on the infection rate of *Botrytis cinerea* using historical climate data (1951–2023) of Central Chile, *Agronomy*, **15**(3), 608.

W. L̃iao, X. Z̃hang, X. L̃iu, M. L̃uo, Y. C̃hen, D. C̃han, et al. (2026) Globally and intergenerationally unequal exposure to hourly heat extremes, *Nature Climate Change*, 1–8.